AGU ADVANCING EARTH AND SPACE SCIENCE

Geophysical Research Letters

RESEARCH LETTER
10.1029/2023GL103883

Key Points:

- First global 3D hybrid simulations to investigate the fate of O^+ ions after escaping the dayside magnetosphere
- New transport/acceleration path for escaped O^+ ions in upstream solar wind region after impact of an IMF tangential discontinuity
- New transport/acceleration path brings some of escaped O^+ ions back to the inner magnetosphere, contributing to O^+ ring current pressure

Supporting Information:

Supporting Information may be found in the online version of this article.

Correspondence to:

C.-P. Wang and X. Wang,
cat@atmos.ucla.edu;
wangxue@auburn.edu

Citation:

Wang, C.-P., Wang, X., & Lin, Y. (2023). Transport and acceleration of O^+ ions in upstream solar wind due to impact of an IMF discontinuity: 3D global hybrid simulation. *Geophysical Research Letters*, *50*, e2023GL103883. https://doi.org/10.1029/2023GL103883

Received 27 MAR 2023
Accepted 16 JUN 2023

Transport and Acceleration of O^+ Ions in Upstream Solar Wind Due To Impact of an IMF Discontinuity: 3D Global Hybrid Simulation

Chih-Ping Wang[1], Xueyi Wang[2], and Yu Lin[2]

[1]Department of Atmospheric and Oceanic Sciences, University of California, Los Angeles, Los Angeles, CA, USA, [2]Physics Department, Auburn University, Auburn, AL, USA

Abstract Based on the predictions of global 3D hybrid simulations, we present a new transport/acceleration path for escaped O^+ ions in the upstream solar wind region resulting from the impact of a particular IMF tangential discontinuity (TD) with negative (positive) IMF B_z on the discontinuity's anti-sunward (sunward) side. For O^+ ions escaping to the duskside magnetosheath and with gyro-radii larger than the TD thickness, when they encounter the TD, they can first go sunward into the upstream solar wind. They then gyrate clockwise to the pre-noon side and get accelerated within the solar wind region and circulate back to the dawnside magnetosphere. These ions may be accelerated to well within the ring current energy range depending on the solar wind electric field strength. This new transport/acceleration path can bring some of the escaped ions into the inner magnetosphere, thus providing a new mechanism for generating an O^+ ring current population.

Plain Language Summary O^+ ions in the magnetosphere only come from the Earth's ionosphere. For O^+ ions escaping the magnetosphere, scientists have been treating them as being lost. Using simulations that can describe the O^+ ion's kinetic dynamics, we find that, due to the impact of a particular solar wind structure, some escaped O^+ ions can circulate back to the magnetosphere via a transport path in the upstream solar wind region and some of them can even enter the inner magnetosphere. Additionally, they are also energized by solar wind electric field and thus can contribute to the ring current population. Therefore, this study shows a new journey of escaped O^+ ions.

1. Introduction

The ionospheric outflow is the sole source for O^+ ions in the magnetosphere. Depending on the outflow locations and energization processes, O^+ ions travel through, populate and interact with different magnetospheric regions. Some O^+ ions may eventually encounter the magnetopause and escape to the magnetosheath and the solar wind (e.g., Armstrong et al., 1978; Cohen et al., 2016; Kronberg et al., 2011; Lee et al., 2020; Sibeck et al., 1987; Slapak et al., 2012, 2015; Zong & Wilken, 1998). Outflows ions are cold (<1 keV) when they come out of the ionosphere. For the O^+ ions traveling within the plasma sheet, they convect sunward and get energized by magnetospheric convection electric field to the plasma sheet energies (from a few keV to ~10 keV) in the tail (e.g., Kistler et al., 2010; Malykhin et al., 2020) and even higher to the ring current energies (from ~10 keV to several hundreds of keV) in the inner magnetosphere ($r < \sim 10\ R_E$) (e.g., Daglis et al., 1993; Lui, 2003; Yue et al., 2018). This transport/acceleration path in the plasma sheet by magnetospheric electric field has been considered as a main mechanism for generating the O^+ ring current population. Once convecting to the dayside magnetopause, O^+ ions may enter the magnetosheath either through an open magnetopause or gyrating across the magnetopause. After escaping into the magnetosheath, some ions may enter the solar wind either through streaming along the magnetic field when the interplanetary magnetic field (IMF) is dominantly radial (Möbius et al., 1986), or, for ions with gyroradius larger than the typical thickness of the magnetosheath (~3 R_E), they can gyrate from the magnetopause to the solar wind (Lee et al., 2020). However, investigating the subsequent journey of these escaped O^+ ions in the magnetosheath or solar wind has never been a focus in past research considering them being lost forever. In this study, we use three-dimensional (3D) global hybrid simulations to present a new transport/acceleration path for escaped O^+ ions in the upstream solar wind region due to the impact of a particular type of IMF directional tangential discontinuity (TD). Additionally, this new path allows some escaped energetic O^+ ions to return to the inner magnetosphere, thus providing a new mechanism for generating an O^+ ring current population.

2. Model and Simulation Description

We use the 3D global hybrid code, AuburN Global hybrId CodE in 3D (ANGIE3D) hybrid code, to simulate the ion dynamics, including H^+ ions from the solar wind and outflow O^+ ions from the ionosphere. The ions, including protons and heavy ions, are treated as discrete, fully kinetic particles, and the electrons are treated as a massless fluid, while a cold, plasmaspheric ion fluid at $r < 6$ R_E is also imposed. Quasi charge neutrality is assumed. Detailed descriptions of the equations for ion particle motion, electric and magnetic fields, and assumptions used in the ANGIE3D code are given in Lin et al. (2014). ANGIE3D has been used to simulate the magnetosphere with the impact of a TD (Lin et al., 2022; Wang et al., 2021a, 2021b, 2022). The code is valid for low-frequency physics with $\omega \sim \Omega_i$ and $k\rho_i \sim 1$ (wavelength $\lambda \sim 6\rho i$), where ω is the wave frequency, k is the wave number, Ω_i is the ion gyrofrequency, and ρ_i is the ion Larmor radius (gyroradius).

For this study, the simulation domain is $20 \geq X \geq -60$, $32 \geq Y \geq -32$, $32 \geq Z \geq -32$ R_E in the geocentric solar magnetospheric (GSM) coordinates. An inner boundary is assumed at the geocentric distance of $r \approx 3$ R_E. The solar wind ion inertial length d_{i0} in this simulation is 0.06 R_E. Note that this d_{i0} value is three times the realistic value. Thus, scaling factors are used when converting the simulation results to realistic magnitudes (Lin et al., 2014; Omidi et al., 2006). Nonuniform cell grids are used, with the grid size (~0.1–0.15 R_E) around the bow shock, magnetosheath, magnetopause, cusp, and equator smaller than in other places. This grid resolution is sufficiently fine for modeling the magnetopause and current sheet. The cell dimensions are $nx \times ny \times nz = 839 \times 500 \times 768$. A total of $\sim 10^{12}$ particles are used. Uniform Pederson conductance of 10 S and Hall conductance of 5 S are specified.

To include the outflow O^+ ions coming out of the ionosphere in ANGIE3D, we adapt the algorithm of Brambles et al. (2010). The outflow ions are specified with four parameters at $r = 2$ R_E: particle flux ($Flux_{outflow}$), parallel bulk flow speed ($V_{\parallel,outflow}$), and parallel temperature ($T_{\parallel,outflow}$) and perpendicular temperature ($T_{\perp,outflow}$). The outflow O^+ fluxes at 4,500 km altitude are specified with the empirical formula of Strangeway et al. (2005), $Flux_{outflow} = 2.14 \times 10^7 S_{\parallel}^{1.265}$, where the flux is in 1/(cm^2-s) and $S_{\parallel}$ is the downward field-aligned DC Poynting flux in mW/m^2. The outflow fluxes are driven self-consistently by the simulated $S_{\parallel}$ flowing from the magnetosphere downward to the ionosphere. Note that we do not restrict the outflow to only the cusp region as in Brambles et al. (2010), thus outflow can also come from other regions, including auroral zone. An M-I coupling module is used to handle the mapping of these parameter values along the dipole magnetic field line between different altitudes from the ionosphere-thermosphere model at $r \sim 1$ R_E to the inner boundary surface at $r = 3$ R_E. For example, the mapping of $Flux_{outflow}$ is determined by conserving $Flux_{outflow}/B_{dip}$, where B_{dip} is the dipole magnetic field strength.

We conducted simulation runs to investigate the impact of a TD on the escaped outflow O^+ ions. H^+ ions are from the solar wind only. For the O^+ outflow ions, time-independent $V_{\parallel,outflow} = 40$ km/s and $T_{\parallel,outflow} = T_{\perp,outflow} = 100$ eV are specified. Initially, there are only H^+ ions and no O^+ ions in the solar wind and magnetosphere. The outflow O^+ ions are initiated at $t = 0$ at the inner boundary with their $Flux_{outflow}$ values changing self-consistently with Poynting fluxes from the magnetosphere. The specified TD is a planar IMF discontinuity with a half-width of 0.3 R_E and the normal direction of (−1, 0, 0). The IMF is purely southward (northward) on the anti-sunward (sunward) side of the TD. The TD plane is located at $X = 262$ R_E at $t = 0$ and convects anti-sunward with the solar wind. We conduct two runs with run 1 under strong solar wind electric field strength and run 2 under moderate strength. The same solar wind density of 5 cm^{-3} and isotropic temperature of 10 eV are specified for both runs. In run 1, the solar wind velocity is (−700, 0, 0) km/s and the IMF is (0, 0, −8) nT on the anti-sunward side of the TD and (0, 0, +8) nT on the sunward side. These magnitudes in run 1 can be seen during solar wind high-speed streams. In run 2, relatively modest values are used with the solar wind velocity of (−400, 0, 0) km/s and the IMF of (0, 0, −4) nT on the anti-sunward side of the TD and (0, 0, +4) nT on the sunward side. The corresponding solar wind electric field in run 1 is thus a factor of 3.5 higher than that of run 2. As shown in Figures S1 and S2 of the Supporting Information S1 for run 1 and 2, respectively, strong O^+ outflow fluxes are mainly in the cusp and nightside aurora regions. O^+ outflow is larger in run 1 than run 2. The peak outflow flux at 100 km is $\sim 1 \times 10^{13}$ (0.1×10^{13}) particles/m^2/s in run 1 (run 2) and the O^+ fluence integrated over one hemisphere is $\sim 0.9 \times 10^{26}$ (0.06×10^{26}) particles/s in run 1 (run 2).

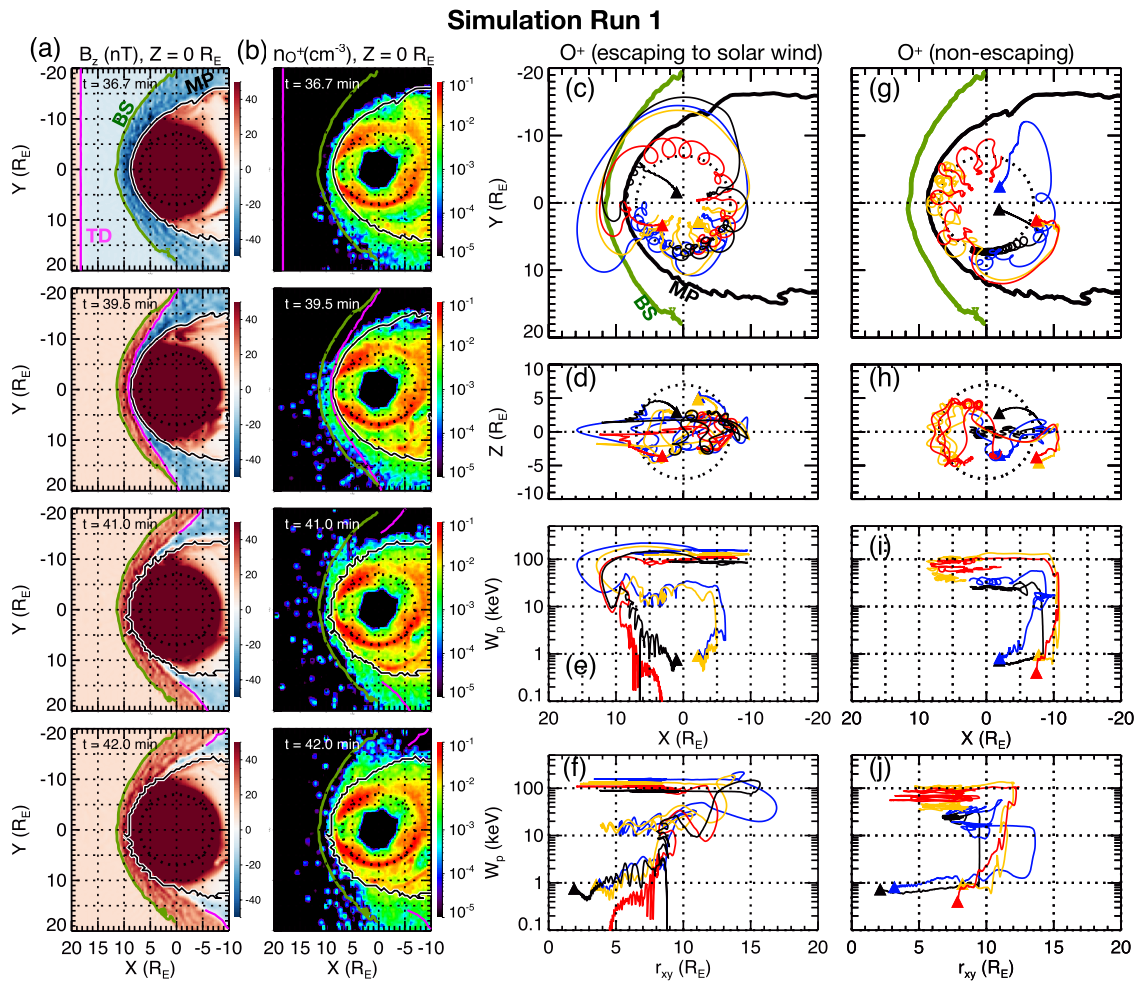

Figure 1. From run 1. The *X-Y* profiles at $Z = 0$ for (a) B_z and (b) O^+ density (n_{O+}) at different times. The bow shock (BS, green curve), the TD (magenta line), and the magnetopause (MP, black curve) are indicated. (c) The *X-Y* and (d) *X-Z* projection of particle trajectory for 4 selected O^+ ions who escape to the upstream solar wind region (each color indicates a particle with starting location marked by a triangle), and the variation of the particle's energy (W_p) along the trajectory with (e) *X*-location and (f) r_{xy}. (g–j) For 4 selected O^+ ions who do not escape the magnetosphere in the same format as (c–f).

3. Simulation Results

We present the run 1 results in Sections 3.1–3.3 and run 2 results in Section 3.4.

3.1. Impact of a TD on Transport Paths of Escaped O^+ Ions

Figures 1a and 1b show time sequences of the spatial distributions of B_z and the O^+ densities (n_{O^+}), respectively, in the *X-Y* (at $Z = 0$) plane from run 1 (also see Movie S1). The nose of the bow shock (green curve) is at $X \sim 12$ R_E, while the nose of the magnetopause (black curve) is at $X \sim 9$ R_E. The TD (magenta line) arrives at the bow shock nose at $t \sim 37.8$ min. As shown in $t = 36.7$ min plots before the TD reaches the bow shock and the IMF in the magnetosheath is still southward, O^+ ions have appeared in the dayside magnetosheath. These O^+ ions escape the magnetosphere due to their relatively larger gyroradius in comparison to the magnetopause thickness. These escaped O^+ ions go farther away from the magnetopause on the duskside than the dawnside and some of them with large gyroradius can reach the upstream solar wind region in the afternoon sector. These escaped O^+ ions all then travel anti-sunward down to the duskside tail magnetosheath. The dawn-dusk asymmetry is mainly due to the duskward electric field in the magnetosheath corresponding to the southward IMF. The impact of the TD on the escaped O^+ ions is seen in the density changes from $t = 39.5$–42.6 min. After the TD enters the magnetosheath, the n_{O+} distributions indicate that some escaped O^+ ions first go sunward to

further upstream from the bow shock on the afternoon side (t = 39.5 min plots), they then move dawnward in the upstream solar wind region to the pre-noon side (t = 41.0 min plots) and later enter the dawnside magnetosheath (t = 42.0 min plots). For the O^+ ions contributing to the n_{O+} distribution changes seen in the upstream solar wind region after the impact of the TD, we select 4 of these ions and plot in Figures 1c and 1d their trajectories (each color indicates one of the particles) on the X-Y and X-Z plane, respectively. Figures 1e and 1f show these particle's kinetic energy ($W_p = 1/2mV_p^2$, where m is the particle's mass and V_p is the particle's velocity) as a function of the particle's X locations and equatorial radial distances ($r_{xy}^2 = X^2 + Y^2$), respectively, along its trajectory. All the trajectories shown in Figures 1c–1f are plotted from t = 27–53 min, and at t = 27 min their locations are all inside $r = 5\ R_E$ with $W_p < 1$ keV (see Figure S3 in Supporting Information S1 for more O^+ trajectories). These trajectories demonstrate that the impact of the TD result in paths for some of the O^+ ions escaping the duskside magnetosphere to travel sunward into the solar wind, then move dawnward in the upstream solar wind region, and eventually circle back to the dawnside magnetosphere. Additionally, some of the O^+ ions can go deeper into the inner magnetosphere and continue drifting westward around the Earth like a typical ring current ion.

3.2. Acceleration of Escaped O^+ Ions in the Solar Wind

The O^+ ions that follow the circulation paths through the upstream solar wind region shown in Figure 1c are accelerated by the solar wind electric field. We select one of the O^+ ions and present in Figure 2 its interaction with the TD and acceleration in the solar wind. Figure 2a shows the X-Y distribution (at $Z = 0$) of B_z at t = 38.5 min (with the trajectory from t = 28–55 min overplotted (color-coded with the ion's W_p values shown in Figure 2i)). Figures 2b–2i show various parameters associated with either the particle or the background fields and plasma along the trajectory from t = 37–47 min. Crossings of the magnetopause is indicated by black vertical dotted lines, the TD by red vertical dashed line, and the bow shock by the black vertical dashed lines, and the regions encountered by the particle are indicated by the bars above Figure 2b (the magnetosphere "MS," the magnetosheath "SH," the solar wind "SW," and the inner magnetosphere "Inner MS"). Figure 2i shows that the particle's W_p is ∼20 keV when it escapes into the duskside magnetosheath around t = 37.9 min. While in the duskside magnetosheath and before it encounters the TD at t = 38.47 min, the particle gyrates counterclockwise (indicated by the particle's velocity component, $V_{p,x}$, $V_{p,y}$, $V_{p,z}$ shown in Figure 2f) since B_z is negative (Figure 2c). Because the magnetosheath E_y is positive at the time (Figure 2e), the particle also gets energized as indicated by positive $\mathbf{E} \cdot \mathbf{V}_p$ values (Figure 2h) from ∼20 to 60 keV (Figure 2i), where $\mathbf{E} \cdot \mathbf{V_p} \propto dW_p/dt$ is particle's energization rate. The energization is mainly in the perpendicular direction, as indicated by α becoming closer to 90° (Figure 2g). The corresponding Larmor radius ρ increases to ∼1 R_E, which is larger than the TD thickness of 0.3 R_E. Hence, when it encounters the TD at t = 38.47 min, it moves across the TD to the upstream side. Once in the TD upstream side region, the particle experiences changes in the directions of B_z, E_x, and E_y (Figures 2c and 2e) since the bulk flow is still anti-sunward (see the components of ion bulk flow $\mathbf{V}_{bulk}$ shown in Figure 2d), which reverses the directions of the electric force ($e\mathbf{E}$, where e is the charge) and magnetic force ($e\mathbf{V}_p \times \mathbf{B}$) in both the X and Y directions. As a result, the particle is pushed sunward (toward the $+X$ direction) and enters the solar wind at $t \sim$ 38.7 min. Since E_y in the region upstream of the TD is negative, as the particle passes the TD and gyrates clockwise with positive $V_{p,y}$ from the magnetosheath to the solar wind, its W_p first decreases to ∼20 keV because $\mathbf{E} \cdot \mathbf{V}_p$ is negative (Figure 2h). But after $t \sim$ 39.5 min when its $V_{p,y}$ becomes negative and thus $\mathbf{E} \cdot \mathbf{V}_p$ becomes positive, its W_p starts to increase. Thus, as the particle gyrates toward the $-Y$ direction and gets energized, the energization further increases its negative $V_{p,y}$ magnitudes and thus increases the positive $\mathbf{E} \cdot \mathbf{V}_p$ magnitudes since E_y is the only electric field component in the solar wind in this simulation run. The energization also increases the particle's gyroradius (note that α remains similar at ∼100°), thus prolonging the Y distance traveled by the particle (moving from $Y \sim$ 13 to $-10\ R_E$) under the negative $V_{p,y}$ before the particle's clockwise gyration eventually brings it back to the pre-noon magnetosheath at t = 42.2 min. As a result, this path within the upstream solar wind region is sufficiently long to energize the O^+ ions by a factor of ∼10 from ∼20 to 200 keV.

The acceleration for the particle presented in Figure 2 well represents the energization experienced by all other O^+ ions traveling in the upstream solar wind region shown in Figure 1c. As shown in Figure 1e, these ions come out from the night region of $0 > X > -5\ R_E$ with $W_p < 1$ keV. They convect sunward in the plasma sheet and get accelerated to ∼10–30 keV by the magnetospheric convection electric field when they encounter the dayside magnetopause and escape. While traveling in the upstream solar wind region (see the trajectories in the region of $X > 10\ R_E$ in Figure 1e), they are further accelerated to ∼100–400 keV.

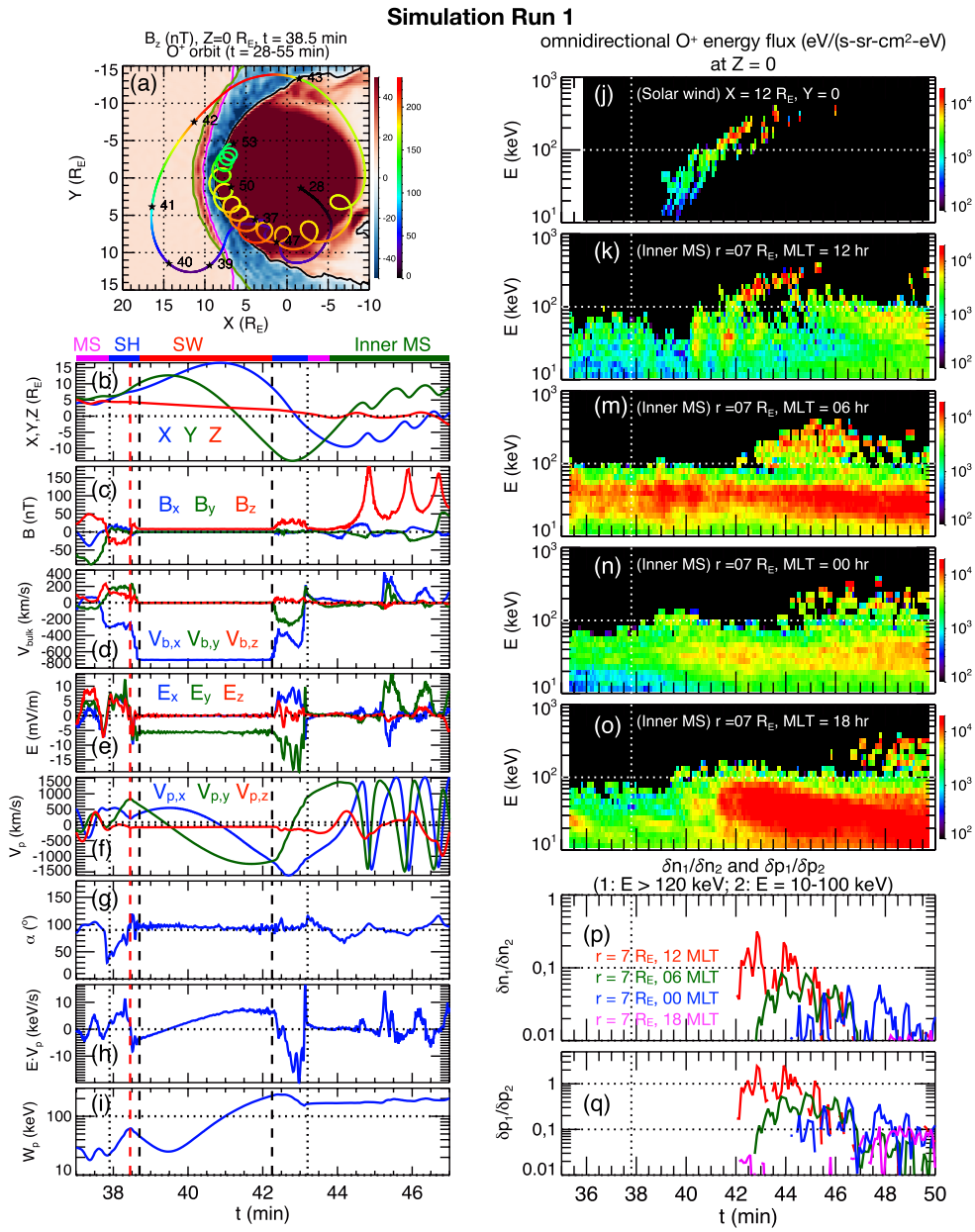

Figure 2. From run 1. (a) The *X-Y* profile of B_z (red-blue color scale) at $Z = 0$ R_E and $t = 38.5$ min overplotted with the trajectory of the example O^+ particle color-coded (rainbow color scale) with the particle's energy (W_p). The bow shock (green curve), TD (magenta curve), and the magnetopause (black curve) are indicated. (b–i) Parameters along the particle's trajectory as a function of time: (b) (*X, Y, Z*) location, (c) magnetic field components, (d) ion bulk flow velocities (V_{bulk}), (e) electric field components, (f) particle velocities (V_p), (g) pitch-angle (α), (h) energization rate ($\mathbf{E}\cdot\mathbf{V}_p$), and (i) W_p. The intervals of solar wind (SW), magnetosheath (SH), magnetosphere (MS), and inner magnetosphere (Inner MS) are indicated by the bars on the top of (b). The crossings of magnetopause (black vertical dotted lines), the bow shock (black vertical dashed lines), and TD (red vertical dotted line) are indicated in (b–i). Energy spectrum of O^+ omnidirectional energy fluxes in (j) the solar wind at (12, 0, 0) R_E and in the inner magnetosphere (MS) at $r = 7$ R_E, $Z = 0$, and MLT = (k) 12, (m) 06, (n) 00, and (o) 18 hr. The ratios of contributions to O^+ (p) density ($\delta n_1/\delta n_2$) and (q) pressure ($\delta p_1/\delta p_2$) in the inner MS at different MLTs. The vertical dotted line indicates TD arrival time.

3.3. Contribution of the Solar-Wind Accelerated O^+ Ions to Ring Current Population

As shown in Figure 1c, the new circulation path due to the impact of the TD bring escaped O^+ ions back to different parts of the magnetosphere, including the inner magnetosphere ($r_{xy} < 10$ R_E). For that O^+ ion shown

in Figure 2a, its energy is ∼200 keV when it enters the inner magnetosphere, and this high energy is achieved while it is accelerated in the upstream solar wind region. This is true for many other ions entering the inner magnetosphere shown in Figure 1c. From their r_{xy}–W_p variations shown in Figure 1f, many of these O^+ ions have $W_p > 100$ keV inside $r_{xy} = 10\ R_E$ and this energy range is reached during their interval within the upstream solar wind. This indicates that the new transport/acceleration path due to the impact of the TD provides a mechanism for adding new ring current O^+ ions to the inner magnetosphere.

For comparison with the escaped O^+ ions, we plot in Figures 1g–1j the trajectories and location-W_p variations for 4 selected O^+ ions that do not escape the magnetosphere and go through transport/acceleration in the plasma sheet by magnetospheric convection electric field. Figures 1i and 1j show that, depending on their trajectories, these ions are accelerated from <1 keV to the range of ∼10–∼100 keV. Comparing Figures 1f and 1j show that the transport/acceleration path in the upstream solar wind region can generate O^+ ring current ions with energies relatively higher than those resulting from the transport/acceleration in the plasma sheet.

We examine in Figures 2j–2o the energy spectrum of O^+ omnidirectional (averaged over all pitch angles) energy fluxes in the solar wind and inner magnetosphere. Figure 2j shows that, shortly after the TD arrives at the bow shock nose (white vertical dotted line), the escaped O^+ ions of ∼10–400 keV pass through the location (12, 0, 0) R_E in the solar wind just in front of the bow shock. There is a dispersion signature with lower energy ions appearing first. Figures 2k–2o show that, before $t \sim 40$ min, there are only O^+ ions of <100 keV in the inner magnetosphere, which is the ring current population resulting from the transport/acceleration in the plasma sheet as shown in Figures 1g–1j. After the impact of the TD, the escaped O^+ ions circulated into the inner magnetosphere shown in Figures 1c–1f resulting in substantial flux increases at > ∼120 keV first at 12 hr MLT (Figure 2k), then 06 hr MLT (Figure 2m), then 00 hr MLT (Figure 2n), and then 18 hr MLT (Figure 2o). These flux increases seen in the inner magnetosphere have the same dispersion signature as that seen in the solar wind (Figure 2j). The predicted energy spectrum can be compared with observations to validate this mechanism. We evaluate the relative importance of the O^+ ring current populations resulting from the two different transport/acceleration paths by comparing the partial densities (δn) and partial pressure (δp) integrated over two energy ranges: (a) δn_1 and δp_1 are integrated over >120 keV for the population due to solar wind acceleration, and (b) δn_2 and δp_2 are integrated over 10–100 keV for the population accelerated in the plasma sheet. Figures 2p and 2q show the ratio of $\delta n_1/\delta n_2$ and $\delta p_1/\delta p_2$, respectively, at 12, 06, and 00 hr MLT. The peak $\delta n_1/\delta n_2$ ratios can be up to ∼0.3 and the peak $\delta p_1/\delta p_2$ ratios up to 2 with the largest ratios seen at 12 MLT and the smallest ratios at 00 MLT. These ratios indicate that the O^+ ring current population resulting from the transport/acceleration in the upstream solar wind region can make a substantial contribution to the O^+ ring current pressure.

3.4. Dependence on the Solar Wind Electric Field

We investigate in Figure 3 whether the new O^+ ion transport/acceleration path in the solar wind due to the TD impact seen in run 1 under a strong solar wind electric field still occur in run 2 under a more moderate electric field (also see Movie S2). As seen in the time sequences of B_z and n_{O^+} distributions shown in Figures 3a and 3b, respectively, and the trajectories and particle energies of selected escaped O^+ ions shown Figures 3c and 3d, respectively, the impact of the TD, which arrives at the bow shock nose at $t \sim 65$ min (note slower solar wind in run 2), is still able to generate the transport/acceleration path in the upstream solar wind region and adding new O^+ ring current ions to the inner magnetosphere (see Figure S4 in Supporting Information S1 for more O^+ trajectories). As shown in Figure 3d, the acceleration in the solar wind can energize the O^+ ions up to ∼80 keV, about a factor of 5 lower than the peak energy of ∼400 keV in run 1. But similar to run 1, the solar wind transport/acceleration path can still add O^+ ring current ions with energies relatively higher than those resulting from the transport/acceleration in the plasma sheet as shown in Figures 3e and 3f. As shown in Figures 3g and 3h, the appearance of O^+ ring current ions resulting from the transport/acceleration in the solar wind can be seen in the increase of fluxes above ∼30 keV first at $t \sim 73$ min at 06 hr MLT then later at 00 hr MLT, in contrast to the 10–20 keV population due to transport/acceleration in the plasma sheet. The contribution from the O^+ ions above 30 keV is substantial as compared to the 10–20 keV population, as can be seen in that the $\delta n_1/\delta n_2$ ratio between these two populations (Figure 3i) can reach peak values of ∼0.3 and the peak $\delta p_1/\delta p_2$ values (Figure 3j) can reach ∼1.

4. Summary

We present a new transport/acceleration path via upstream solar wind region for escaped O^+ ions due to the impact of a particular type of TD predicted by global 3D hybrid simulations. The TD has southward (northward) IMF on its downstream (upstream) side. Before the arrival of the TD, the O^+ ions escaping the dayside

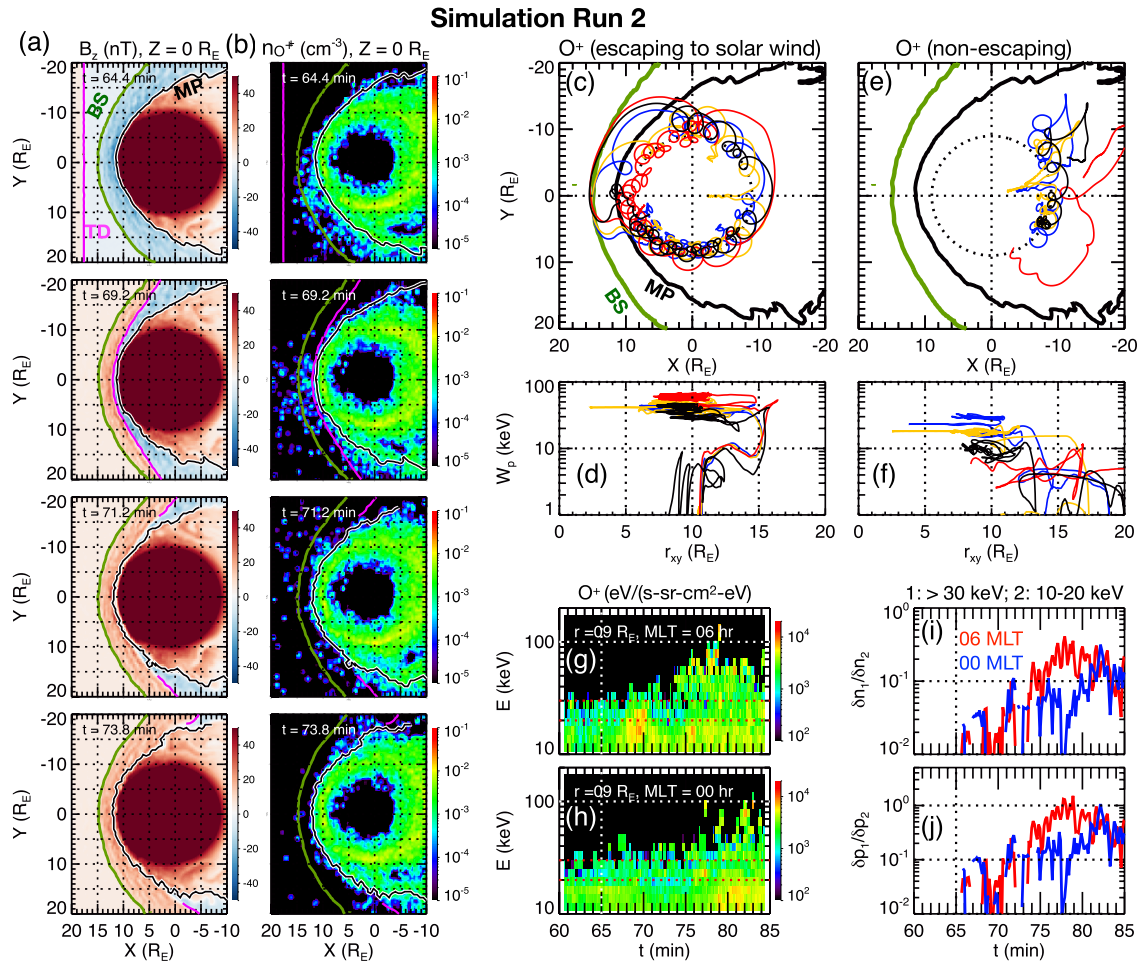

Figure 3. From run 2. The *X-Y* profiles at $Z = 0$ for (a) B_z and (b) n_{O+} at different times. The bow shock (BS, green curve), the TD (magenta line), and the magnetopause (MP, black curve) are indicated. (c and e) The *X-Y* and (d and f) W_p–r_{xy} along the trajectory of 4 selected O^+ ions who escape to the upstream solar wind region (each color indicates a particle starting location marked by a triangle) (c–d) and 4 selected O^+ ions who do not escape the magnetosphere (e–f). Energy spectrum of O^+ omnidirectional energy fluxes in the inner magnetosphere at $r = 9\ R_E$, $Z = 0$, and MLT = (g) 06, and (h) 00 hr. The ratios of contributions to (i) O^+ density ($\delta n_1/\delta n_2$) and (j) pressure ($\delta p_1/\delta p_2$) at 06 and 00 hr MLT. The vertical dotted line indicates TD arrival time.

magnetosphere can only flow anti-sunward to the tail magnetosheath. When escaped O^+ ions encounter the TD in the afternoon side magnetosheath and experience the field reversal across the TD, they can first move sunward into the solar wind, gyrate clockwise in the solar wind to the pre-noon side and get accelerated, and then some of them can return to the dawnside magnetosphere or even into the inner magnetosphere. They can be accelerated in the solar wind to within the typical ring current energy range of $> \sim$10 keV to several hundreds of keV depending on the solar wind electric field strength. Thus, this new path via the upstream solar wind region serves a new mechanism to add ring current O^+ ions, in addition to those resulting from the transport/acceleration in the plasma sheet. Additionally, the contribution to the O^+ ring current pressure from this new mechanism can be substantial based on the two simulation runs. Future studies are certainly needed to expand investigations of this path/mechanism, including validating it by comparing the predicted energy spectrum with observations, and more appropriately evaluating its contribution to storm-time ring current during different storm phases by conducting simulations with more realistic conditions.

Data Availability Statement

The simulation data can be found at https://figshare.com/articles/dataset/Circulation_and_energization_of_O_ions_through_upstream_solar_wind_region/21266661.

Acknowledgments
C.-P. Wang is supported by NASA 80NSSC22K1012 and NSF-GEM 2224108. Xueyi Wang and Yu Lin are supported by NASA 80NSSC22K1012 and NSF-GEM 2224109.

References

Armstrong, T. P., Krimigis, S. M., & Lepping, R. P. (1978). Magnetosheath bursts of predominantly medium nuclei observed with Imp 8 on February 16, 1974. *Journal of Geophysical Research*, *83*(A11), 5198–5206. https://doi.org/10.1029/JA083iA11p05198

Brambles, O. J., Lotko, W., Damiano, P. A., Zhang, B., Wiltberger, M., & Lyon, J. (2010). Effects of causally driven cusp O^+ outflow on the storm time magnetosphere-ionosphere system using a multifluid global simulation. *Journal of Geophysical Research*, *115*(A9), A00J04. https://doi.org/10.1029/2010JA015469

Cohen, I. J., Mauk, B. H., Anderson, B. J., Westlake, J. H., Sibeck, D. G., Giles, B. L., et al. (2016). Observations of energetic particle escape at the magnetopause: Early results from the MMS Energetic Ion Spectrometer (EIS). *Geophysical Research Letters*, *43*(12), 5960–5968. https://doi.org/10.1002/2016GL068689

Daglis, I. A., Sarris, E. T., & Wilken, B. (1993). AMPTE/CCE observations of the ion population at geosynchronous altitudes. *Annales de Geophysique*, *11*, 685–696.

Kistler, L. M., Mouikis, C. G., Klecker, B., & Dandouras, I. (2010). Cusp as a source for oxygen in the plasma sheet during geomagnetic storms. *Journal of Geophysical Research*, *115*(A3), A03209. https://doi.org/10.1029/2009JA014838

Kronberg, E. A., Bučík, R., Haaland, S., Klecker, B., Keika, K., Desai, M. I., et al. (2011). On the origin of the energetic ion events measured upstream of the Earth's bow shock by STEREO, Cluster, and Geotail. *Journal of Geophysical Research*, *116*(A2), A02210. https://doi.org/10.1029/2010JA015561

Lee, S. H., Sibeck, D. G., Lin, Y., Guo, Z., Adrian, M. L., Silveira, M. V. D., et al. (2020). Characteristics of escaping magnetospheric ions associated with magnetic field fluctuations. *Journal of Geophysical Research: Space Physics*, *125*(4), e2019JA027337. https://doi.org/10.1029/2019JA027337

Lin, Y., Wang, X., Sibeck, D. G., Wang, C.-P., & Lee, S.-H. (2022). Global asymmetries of hot flow anomalies. *Geophysical Research Letters*, *49*(4), e2021GL096970. https://doi.org/10.1029/2021GL096970

Lin, Y., Wang, X. Y., Lu, S., Perez, J. D., & Lu, Q. (2014). Investigation of storm time magnetotail and ion injection using three-dimensional global hybrid simulation. *Journal of Geophysical Research: Space Physics*, *119*(9), 7413–7432. https://doi.org/10.1002/2014JA020005

Lui, A. T. Y. (2003). Inner magnetospheric plasma pressure distribution and its local time asymmetry. *Geophysical Research Letters*, *30*(16), 1846. https://doi.org/10.1029/2003GL017596

Malykhin, A. Y., Grigorenko, E. E., Kronberg, E. A., & Daly, P. (2020). Variations in ion-component pressure during dipolarization in the near-earth magnetotail plasma sheet. *Geomagnetism and Aeronomy*, *60*(1), 20–27. https://doi.org/10.1134/S0016793220010090

Möbius, E., Hovestadt, D., Klecker, B., Scholer, M., Ipavich, F. M., Carlson, C. W., & Lin, R. P. (1986). A burst of energetic O^+ ions during an upstream particle event. *Geophysical Research Letters*, *13*, 1372–1375. https://doi.org/10.1029/gl013i013p01372

Omidi, N., Blanco-Cano, X., Russell, C. T., & Karimabadi, H. (2006). Dipolar magnetospheres and their characterization as a function of magnetic moment. *Advances in Space Research*, *33*(11), 1996–2003. https://doi.org/10.1016/j.asr.2003.08.041

Sibeck, D. G., McEntire, R. W., Lui, A. T. Y., Lopez, R. E., Krimigis, S. M., Decker, R. B., et al. (1987). Energetic magnetospheric ions at the dayside magnetopause: Leakage or merging? *Journal of Geophysical Research*, *92*(A11), 12097–12114. https://doi.org/10.1029/JA092iA11p12097

Slapak, R., Nilsson, H., Westerberg, L. G., & Eriksson, A. (2012). Observations of oxygen ions in the dayside magnetosheath associated with southward IMF. *Journal of Geophysical Research: Space Physics*, *117*(A7), A07218. https://doi.org/10.1029/2012ja017754

Slapak, R., Nilsson, H., Westerberg, L. G., & Larsson, R. (2015). O^+ transport in the dayside magnetosheath and its dependence on the IMF direction. *Annals of Geophysics*, *33*(3), 301–307. https://doi.org/10.5194/angeo-33-301-2015

Strangeway, R. J., Ergun, R. E., Su, Y.-J., Carlson, C. W., & Elphic, R. C. (2005). Factors controlling ionospheric outflows as observed at intermediate altitudes. *Journal of Geophysical Research*, *110*(A3), A03221. https://doi.org/10.1029/2004JA010829

Wang, C.-P., Wang, X., Liu, T. Z., & Lin, Y. (2021a). A foreshock bubble driven by an IMF tangential discontinuity: 3D global hybrid simulation. *Geophysical Research Letters*, *48*(9), e2021GL093068. https://doi.org/10.1029/2021GL093068

Wang, C.-P., Wang, X., Liu, T. Z., & Lin, Y. (2021b). Impact of foreshock transients on the flank magnetopause and magnetosphere and the ionosphere. *Frontiers in Astronomy and Space Sciences*, *8*, 160. https://doi.org/10.3389/fspas.2021.751244

Wang, C.-P., Xing, X., Wang, X., Avanov, L. A., Lin, Y., Strangeway, R. J., & Wei, H. Y. (2022). Effect of IMF *By* on the entry of solar wind ions into the near-Earth tail lobe: Global hybrid simulation and MMS observation. *Journal of Geophysical Research: Space Physics*, *127*, e2022JA030800. https://doi.org/10.1029/2022JA030800

Yue, C., Bortnik, J., Li, W., Ma, Q., Gkioulidou, M., Reeves, G. D., et al. (2018). The composition of plasma inside geostationary orbit based on Van Allen Probes observations. *Journal of Geophysical Research: Space Physics*, *123*(8), 6478–6493. https://doi.org/10.1029/2018JA025344

Zong, Q.-G., & Wilken, B. (1998). Layered structure of energetic oxygen ions in the dayside magnetosheath. *Geophysical Research Letters*, *25*(22), 4121–4124. https://doi.org/10.1029/1998GL900110